A study on cavitation erosion behavior of AlSi10Mg fabricated by selective laser melting (SLM)

J. Zou[1,†], Y. Zhu[1,*,†], M. Pan[2], T. Xie[1], X. Chen[1], H. Yang[1]

1: State key laboratory of fluid power and mechatronic systems, Zhejiang University, Zheda Road 38, 310027 Hangzhou, China

2: Department of mechanical engineering, University of Bath, BA2 7AY Bath, the UK

*: Corresponding author. Y. Zhu Tel: +86 18694580181; fax: +86 57187951941; e-mail: yiz@zju.edu.cn

†: both authors contribute equally to the paper

ABSTRACT

Cavitation erosion causes serious problems for hydraulic machinery. Selective laser melting (SLM), is a type of additive manufacturing that can produce metal parts directly and it has begun to be used in various industrial settings. However, the erosion properties of the SLM processed parts have only rarely been reported. The paper addresses the cavitation erosion behavior of AlSi10Mg samples fabricated by SLM at different laser scanning speeds. A wrought sample was also tested to provide a basis for comparison. Sample hardness and microstructure were investigated. Results showed the cavitation erosion behaviors of SLM samples to differ greatly from that of the wrought sample. The erosion rate of SLM samples was found to peak in the first 30 s. This was accompanied by the removal of particles inside pores. After peaking, the erosion rate of the SLM samples decreased significantly. SLM samples showed an extremely low erosion rate entering the steady-state period. Large, deep craters which were common wear marks on the wrought sample, were not present on the SLM samples. Different scanning speeds resulted in different max erosion rates.

Keywords: Cavitation erosion; surface topography; intermetallics; other manufacturing processes

1. Introduction

Cavitation is the explosive growth and intense collapse of bubble nuclei in liquid exposed to large pressure variations [1]. Cavitation erosion can reduce the performance of components and shorten

lifetime owing to failure, particularly in hydraulic machinery, such as pumps and valves. There are two main sources of cavitation, both of which are caused by a vibratory machine or the use of a high-speed water jet. The details can be found according to two international standard erosion tests ASTM G32 and ASTM G134. Many studies have focused on factors influencing cavitation erosion resistance, such as material properties [2–5], flow velocity [2], cavitation intensity [3], nozzle geometry[4], fluid media [6], water temperature [7], and surface topography [8,9]. In addition, some studies have focused on the mechanisms of cavitation erosion caused damage [10–12] and on tracking the progress of damage over cavitation time [13–15].

Selective laser melting (SLM) is one type of additive manufacturing (AM) technology. It is based on a laser beam scanning various layers of deposited metal powder according to the sliced CAD model and selectively melting the metal powder under controlled conditions. A review of the SLM technology including machine characteristics and material microstructure was published by Uriondo et al. [16]. AlSi10Mg alloys are widely used for their good weldability, hardenability, and excellent corrosion resistance. Due to the unique layer-by-layer process of SLM, the microstructure and mechanical properties of the parts differed considerably from conventional casting or forging. Thijs et al. [17] investigated the AlSi10Mg parts produced by various scanning strategies and found a very fine microstructure with submicron-sized cells leading to high hardness due to the high thermal gradient that occurred during SLM process. In addition, a characteristic morphological and crystallographic texture was present due to the unique solidification conditions and the additive character of the process. Similarly, Manfredi et al. [18] evaluated the microstructural and mechanical properties of SLM processed AlSi10Mg and found SLM parts had far higher yield strength than as-cast parts. A very fine cellular-dendritic structure was also reported. Kempen et al. [19] concluded that the mechanical properties of SLM processed AlSi10Mg were comparable or even greater than those of cast components including tensile strength, elongation, impact toughness, and hardness. Read et al. [20] compared SLM parts produced under different sets of parameters and optimum process parameters were identified. Brandl et al. [21] evaluated the fatigue performance of the SLM parts and found the fatigue resistance was high in SLM samples. The post heat treatment had the most considerable effect and the building direction had the least considerable effect on the fatigue resistance.

However, the manner in which the unique microstructure and mechanical properties caused by the SLM

process affect the cavitation erosion has not been investigated. Cottam et al. [11] performed a cavitation erosion test comparing two types of laser surface treatments on nickel-aluminum bronze, laser surface melting, and laser processing. Results showed that the tensile residue stresses in the laser melted sample weakened the sample, though it was still stronger than the laser processed sample. Nevertheless, SLM, which is a manufacturing process, is different from laser surface melting, which is a surface treatment. The laser scanning strategy is more complex during SLM than other processes and the deforming behaviors of the SLM parts are notably different.

In this study, cavitation erosion tests were performed on AlSi10Mg parts that had been processed by SLM at different scanning speeds. A wrought sample was also tested in order to provide a basis for comparison. Microstructures were examined, and the changes in surface topography on the same area during cavitation erosion were recorded. The cavitation erosion behaviors of the SLM parts were very different from the wrought AlSi10Mg sample. The mechanism of the damage on the eroded surface was discussed.

2. Experimental details

2.1 SLM process

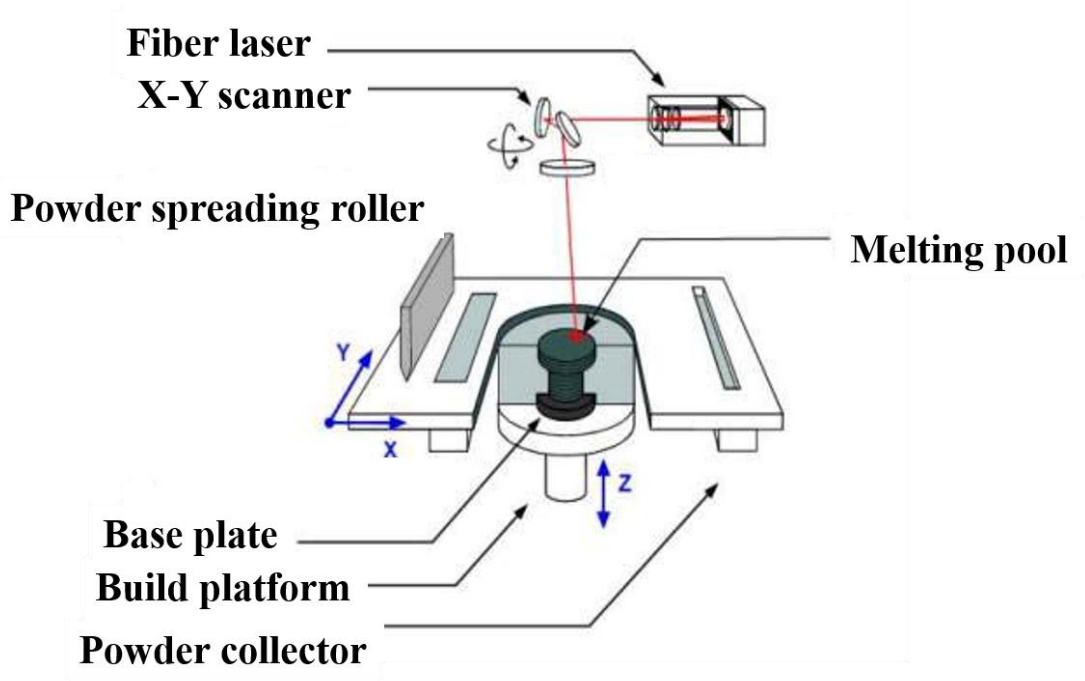

Fig. 1 Schematic of the SLM system [19]

SLM was performed using a Concept Laser M2 cusing laser melting unit comprised of a 400 W ytterbium fiber laser, an automatic powder layering system, a gas protection system, and a process control system. The laser operated with a 50 μm focused beam diameter. A schematic of the SLM system is shown in Fig. 1. The laser power applied for all three SLM parts was 370 W while the scanning speeds had three levels. A standard scanning speed (1300 mm/s) was applied to sample A; 0.4× standard scanning speed (520 mm/s) was applied to sample B, and 2× standard scanning speed (2600 mm/s) was applied to sample C. The sealed working chamber was fed with high-purity argon, and the oxygen content was reducible to below 100 ppm. Each powder layer was scanned by the laser to build up the sample according to a predefined CAD model. The AlSi10Mg powders were spherical in shape, having diameters distributed in the range of 20 μm to 60 μm with an average particle diameter of 30 μm.

2.2 Sample preparation and material characterization

All SLM and wrought samples (sample D) had a dimension of 20 mm × 20 mm × 10 mm, and the composition of the samples is listed in Table. 1. The SLM samples were not subjected to any heat treatments. In order to eliminate the influence of the surface topography on cavitation erosion, all samples were polished with R_a = 0.05 μm before the experiment.

The densities of the SLM samples and wrought sample were measured based on Archimedes' principle. The macro-hardness of each sample was measured using a Vickers hardness tester with a 200 g load. Mean values were obtained from six measurements conducted on a single sample. The nano-hardness was measured using a Keysight Nano Indenter G200, which involved using a Berkovich indenter with a tip radius of 20 nm. Material phase identification was performed by x-ray diffraction (XRD). Metallographic examination was performed using optical microscopy and scanning electron microscopy (SEM) on polished and etched cross sections. The surface topography was observed using confocal laser scanning microscopy (CLSM; VK-150 Keyence Corp.) which features the acquisition of in-focus images from selected depths, which is called optical sectioning.

Table 1. Chemical composition of the AlSi10Mg alloy

Element	Al	Si	Cu	Mn	Mg	Zn	Fe
wt%	Balanced	9－11	≤0.05	≤0.45	0.2－0.45	≤0.10	≤0.55

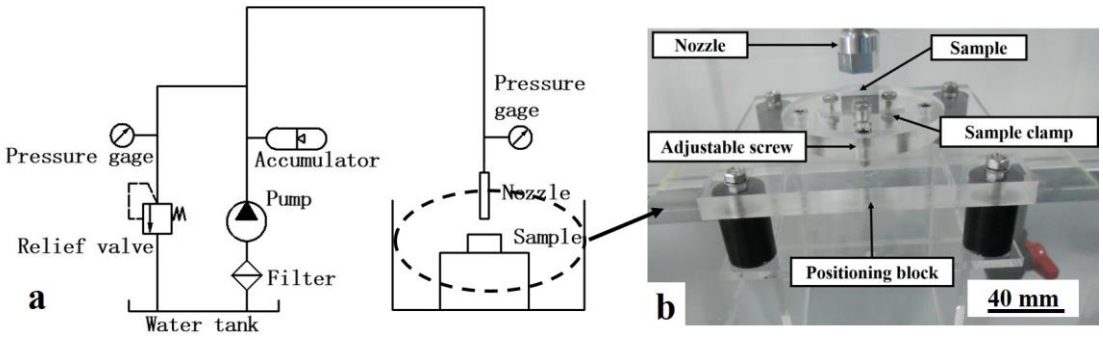

Fig. 2 Cavitation erosion test setup. (a) Schematic diagram of the cavitation apparatus; (b) a photo of the mounted sample.

2.3 Test rig and test procedure

The cavitation erosion test was conducted on a rig designed according to the ASTM G134 standard. The test setup is shown schematically in Fig. 2, and an image of the rig is also showed. The water is pressurized by a pump and injected through a nozzle into the test section which is filled with water. The sample is fixed by clamps mounted on a platform, which is set perpendicular to the nozzle. The distance between the nozzle and the sample is adjusted using screws in order to determine the stand-off distance, shown in Fig. 2 (b). The rig employs a standard ASTM G134 nozzle [3]. Tap water maintains at a temperature of 20 ± 2ºC served as the test liquid. The pressure of the water pump is set to 16 MPa.

In cavitation erosion tests, the distance between the tip of the nozzle and sample surface is crucial. The optimum stand-off distance is the position where the amount of mass lost peaks [2]. Therefore, a preliminary test was conducted using pure aluminum to determine the optimum stand-off distance at a flow velocity of 147 m/s. Fig. 3 shows the relationship between the stand-off distance and the mass loss of samples after 20 min of cavitation erosion testing. It can be easily determined that the optimum stand-off distance used for the current test set-up was 18 mm.

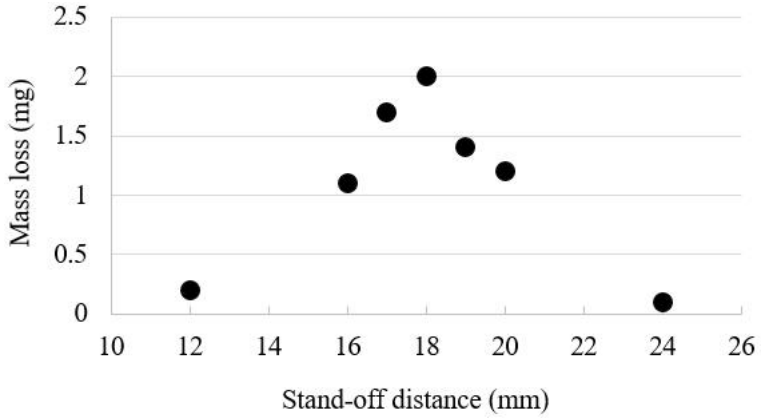

Fig. 3 Determination of the optimum stand-off distance.

The samples were subjected to cavitation erosion testing for predetermined periods and the weight lost was recorded after ultrasonic cleaning with acetone for 10 min. Each test was repeated once. In order to track the changes in surface topography and surface damage due to cavitation erosion, an area of 1000 μm × 1394 μm was continuously measured using CLSM. Measurement intervals are shown in Fig. 8. Different intervals were used for the SLM and wrought samples since samples manufactured by different processes have very different cavitation erosion behaviors. The mass loss of the specimen was recorded using an analytical balance with a 0.1 mg resolution. Each sample was weighed 6 times.

3. Results

3.1 Material characteristics

The CLSM graphs of the cross sections of 4 samples are shown in Fig. 4. SLM samples have microstructures very different from those of the wrought sample. All SLM samples have crescent molten pools in the cross section indicating laser scanning tracks. However, pores are observed on all SLM samples, which are hard to completely eliminate in the SLM process. Many studies were performed to investigate the relationship between the laser process parameters and the number of pores and further linked to the mechanical properties [16,22–25]. There are fewer pores in the SLM A sample than in the other two indicating scanning speeds have a pronounced influence on the material densification. These pores differ in size and morphology, which have several causes: (1) the balling effect [26], (2) residual oxygen in the building chamber, and (3) imperfections in the powders [22].

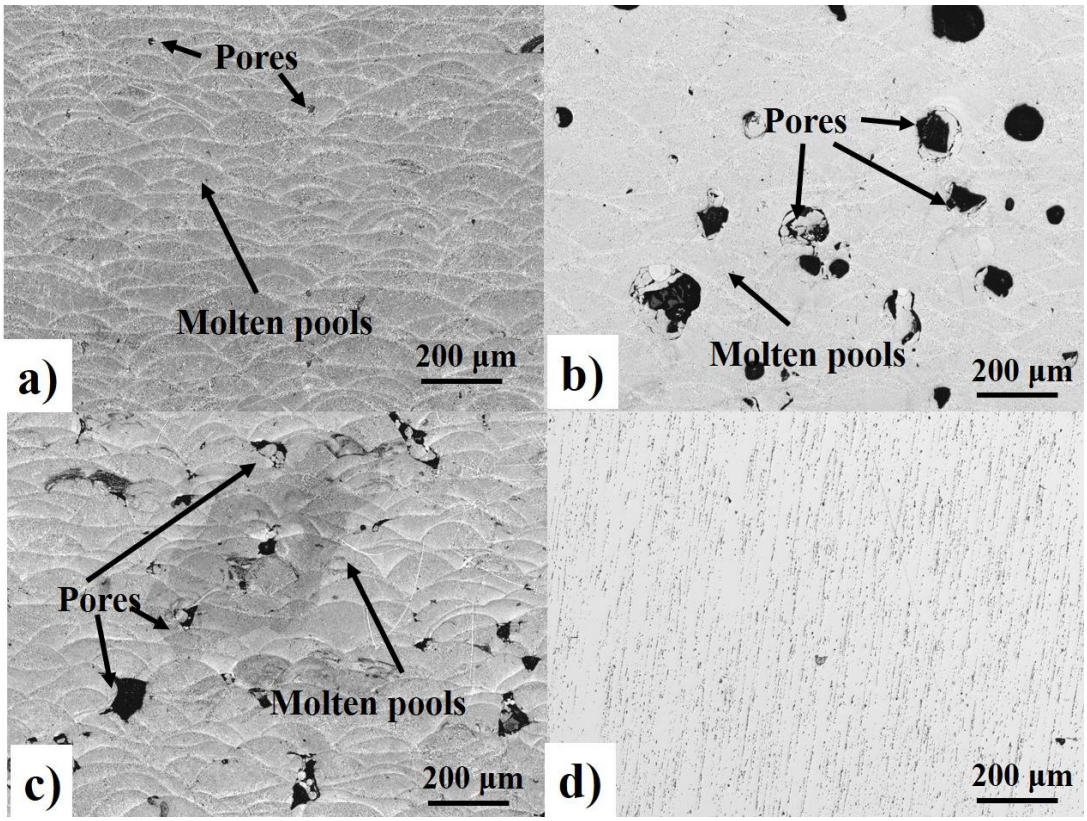

Fig. 4 CLSM graphs of cross sections of 4 samples: (a) A SLM 1; (b) B SLM 0.4; (c) C SLM 2 and (d) D wrought.

Table. 2 Hardness and densities (mean value of 6 measurements at each sample) of 4 samples.

Sample	A_SLM 1	B_SLM 0.4	C_SLM 2	D
Laser scanning speed (mm/s)	1300	520	2600	-
Hardness (HV)	124.4	120.0	121.2	100.3
Densification (%)*	95.85	90.85	92.96	100

*: densification of the SLM samples was here calculated as the density of the SLM sample divided by the density of sample D.

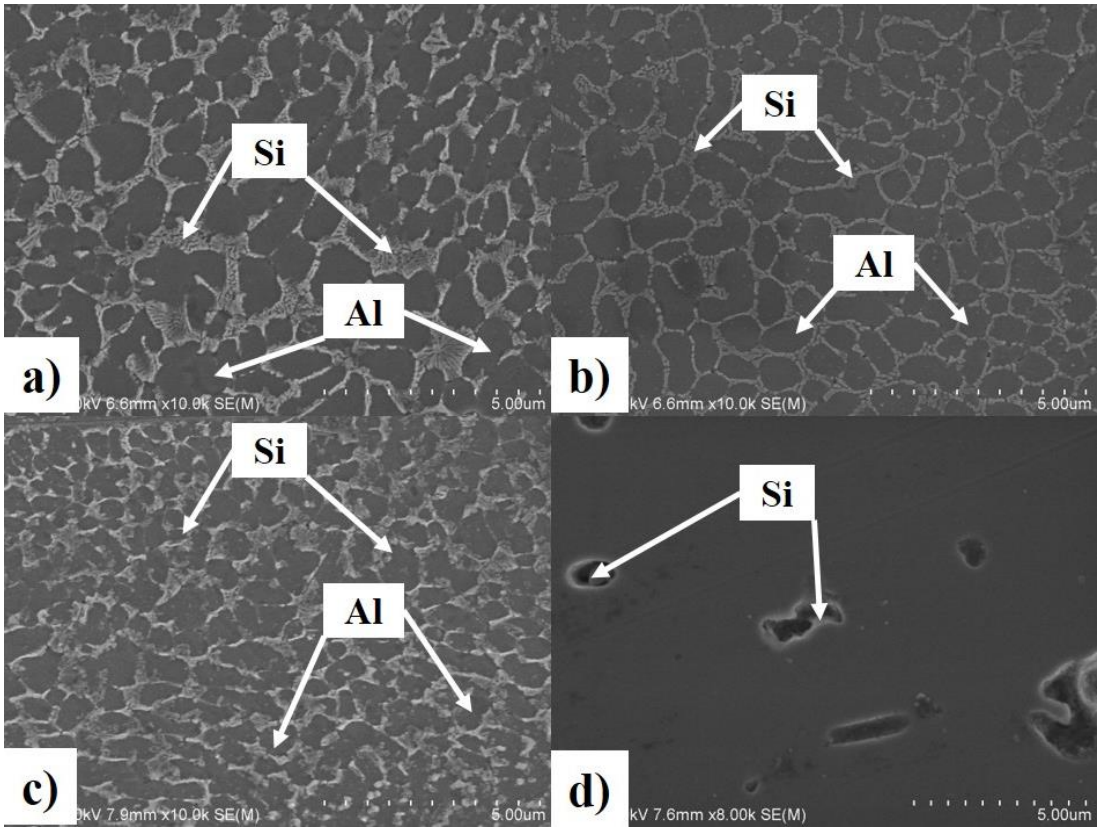

Fig. 5 SEM graphs of samples at top view: (a) A_SLM 1; (b) B_SLM 0.4; (c) C_SLM 2; and (d) D.

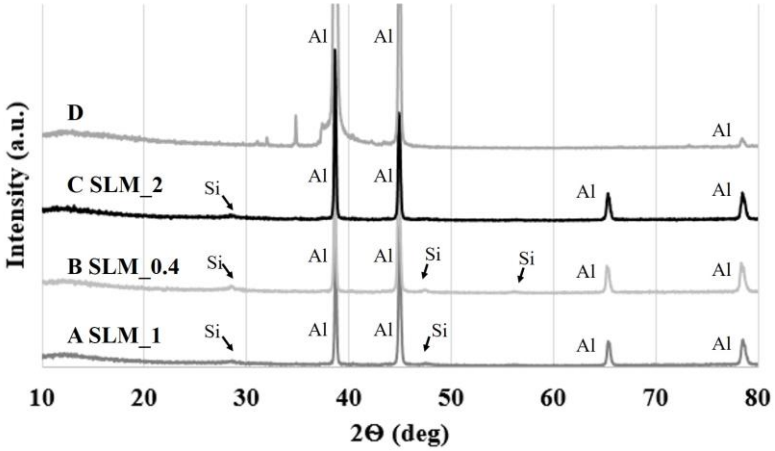

Fig. 6 XRD results of 4 samples.

The pores reduce the overall density of the component. The densities and macro-hardness of 4 samples are listed in Table 2. Sample A shows the highest density of the three SLM samples. The ranking of the densities of the three SLM samples is consistent with the cross-section observation. The difference in hardness between SLM samples is small. The hardness of the wrought sample is similar to the sample made using high pressure die casting F [19]. The high hardness of the SLM samples results from the

fine grains due to rapid cooling and heating rate [18,22].

The SEM graphs of samples are shown in Fig. 5. Very fine cellular-dendritic structures are found on three SLM samples, which differ greatly from sample D. More silicon particles can be observed from SLM samples than the wrought sample. The structure of the SLM samples features primary Al (dark shading) and fibrous Si particles (bright). The observation is in line with results published in [17–19,27]. The grains are less than 1 μm in size, which vary only slightly among three SLM samples. Results have shown that the network of structures is broken at some places. This is because that the heat is not very uniformly diffused during laser scanning. This causes the microstructures of the SLM-built samples to be different in different parts of the sample. The results of XRD analysis are shown in Fig. 6. Aluminum peaks are strong for all samples, though the SLM samples shows more silicon peaks than the wrought sample. This indicates that more silicon has been precipitated from the aluminum matrix, which is consistent with SEM observations.

3.2 Mass loss of cavitation erosion

Fig. 7 shows the cumulative mass loss versus time for 4 samples. Results indicate the SLM samples have the similar trends but different values. The mass of all SLM samples decreases very quickly in the first 10 min, then increases slightly and remains nearly stable. The SLM sample with standard scanning speed shows that the lowest mass loss, while the SLM sample with low scanning speed has the highest mass loss. The mass of the wrought sample first decreases slowly and then begins to increase steadily. The mass loss curve of the wrought sample is consistent with the finding of a previous study [9], which differs from the SLM samples.

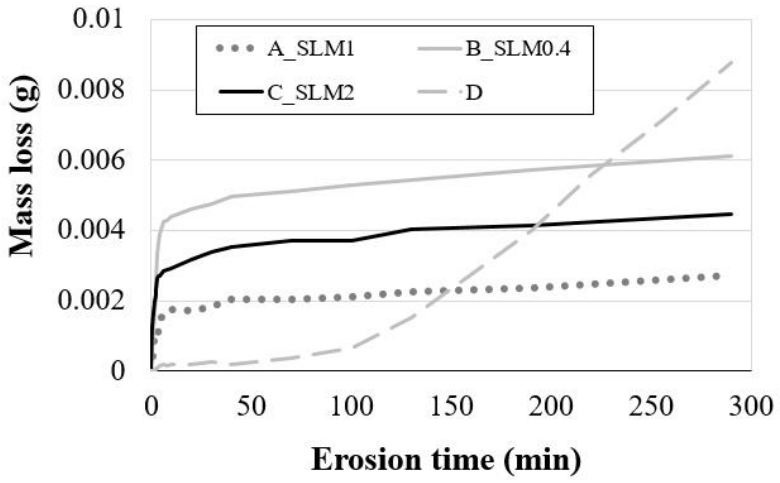

Fig. 7 Cumulative mass loss (mean value) versus time for 4 samples. Tests were performed twice.

The mass loss rate curve is often used to characterize erosion behaviors of various materials. The curves of mass loss rate here are derived from the cumulative mass loss curve. $\frac{dm}{dt}$ is the mass lost during each measurement interval (m_{t-1}-m_t) divided by the time interval Δt. It is commonly accepted that material erosion progresses through the following stages: incubation period; acceleration period; deceleration period; and steady-state period [1]. Fig. 8 shows the mass loss rates of 4 samples. Similarly, three SLM samples show curves with a similar pattern while the wrought sample has a different curve. During the first 30 s, the mass loss rate of SLM samples peaks and no incubation period is observed. After peaking, the rate reduces greatly, which can be recognized as the deceleration period. After 10 min, the mass loss rates of all SLM samples are less than 1/20 of the peak value. The mass loss rate in the steady-state period is extremely low (below 0.01 mg/min). The influence of the scanning speeds is observed on the peak value of the mass loss rate and the duration of the deceleration period (Table 2). However, the wrought sample clearly shows four stages. The incubation period is short (approximately 1 min). Then the erosion rate of the wrought sample starts to accelerate for approximately 4 hours. After a short deceleration period, the mass loss rate remains stable at approximately 0.045 mg/min. Some important values are listed in Table 3 to facilitate better comparison among 4 samples.

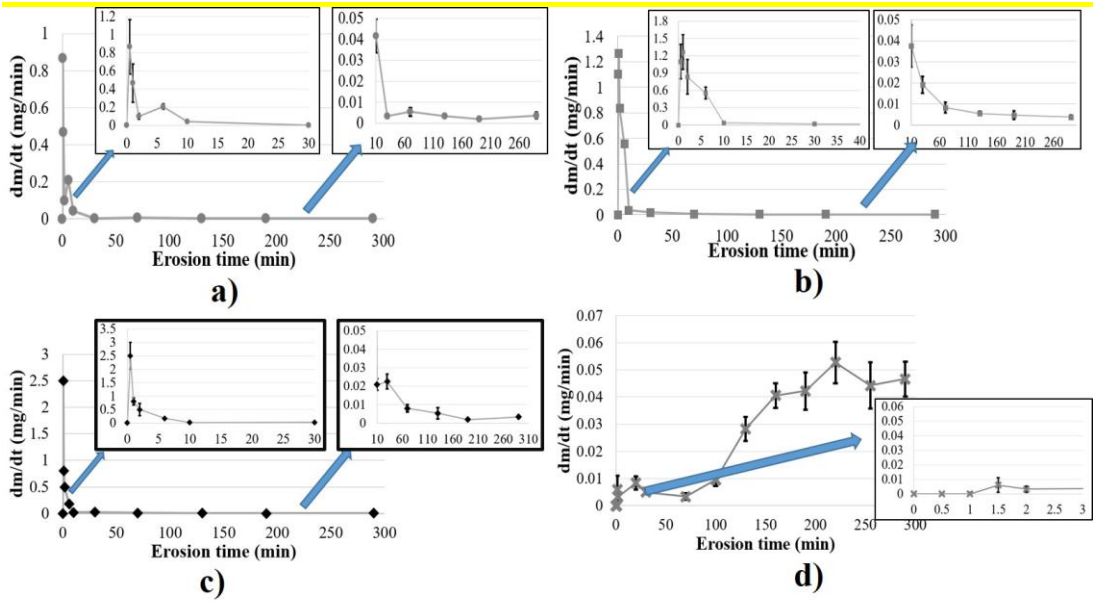

Fig. 8 Mass loss rate (mean value and standard deviation) of 4 samples. Tests were performed twice. a) sample A; b) sample B; c) sample C; and d) sample D.

Table 3. Values (mean value) from curves of mass loss rate of 4 samples. Tests were performed twice.

Sample	Max mass loss rate (mg/min)	Time to reach max mass loss rate (min)	Rate of mass loss at the steady-state period (mg/min)	Time required to reach the steady-state period (min)
A_SLM 1	0.87	0.5	0.0035	30
B_SLM 0.4	1.27	0.5	0.0056	60
C_SLM 2	2.5	0.5	0.0046	60
D	0.05	220	0.046	250

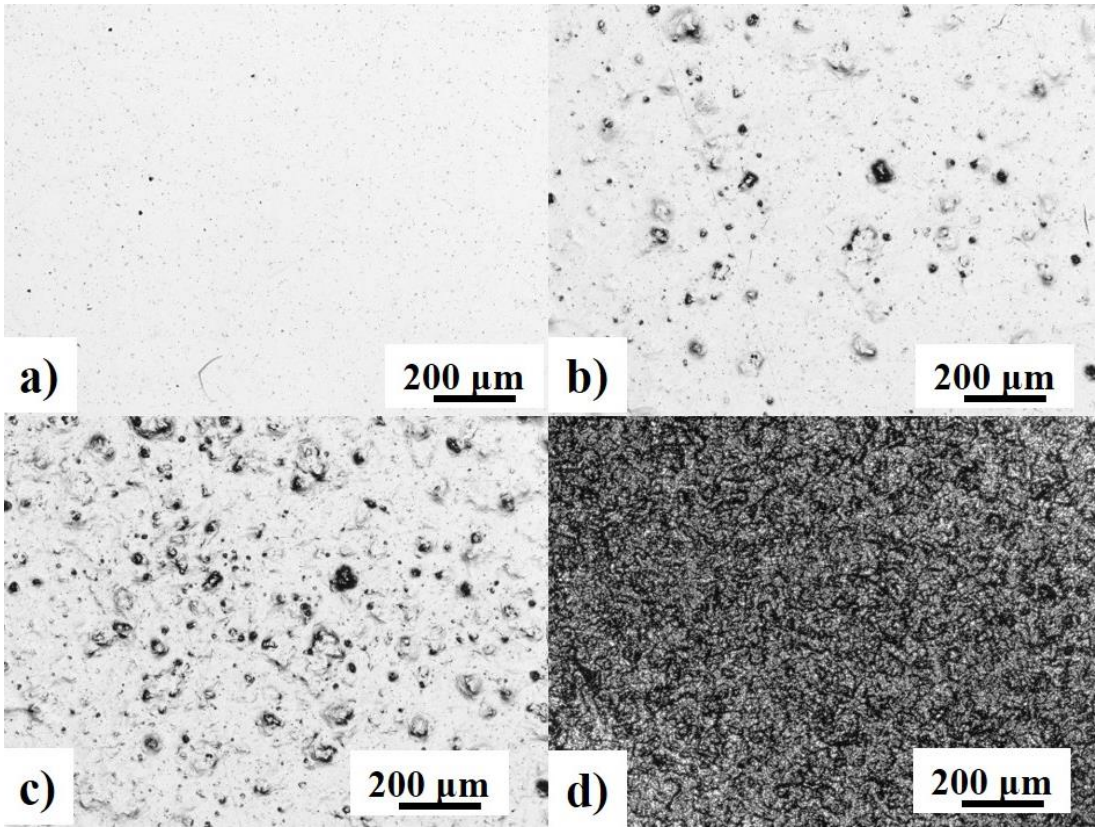

Fig. 9 Surface topography tracking of sample D observed at (a) the original state; (b) after 30 s; (c) after 1.5 min, and (d) after 20 min.

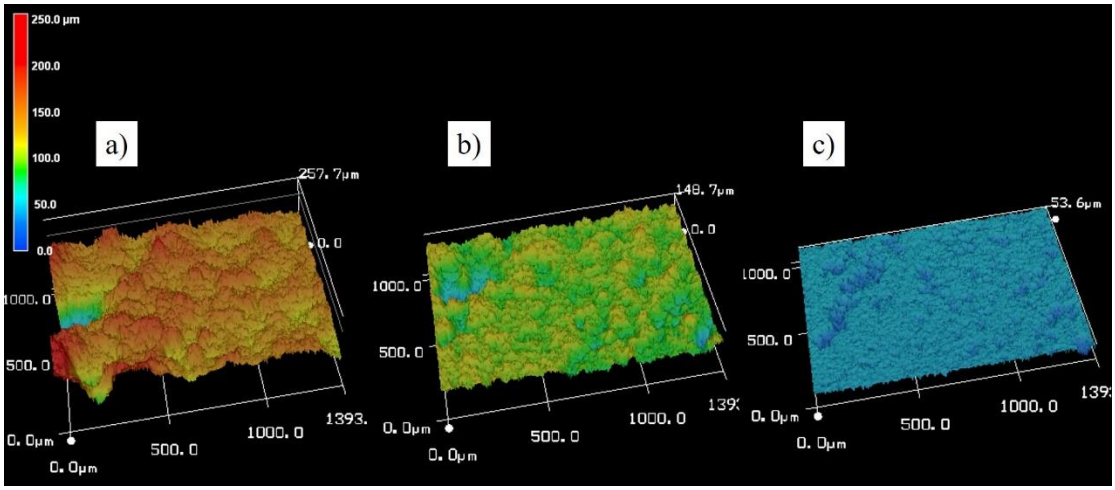

Fig. 10 3D surface topography of sample D measured by CLSM at (a) 290 min; (b) 100 min, and (c) 70 min.

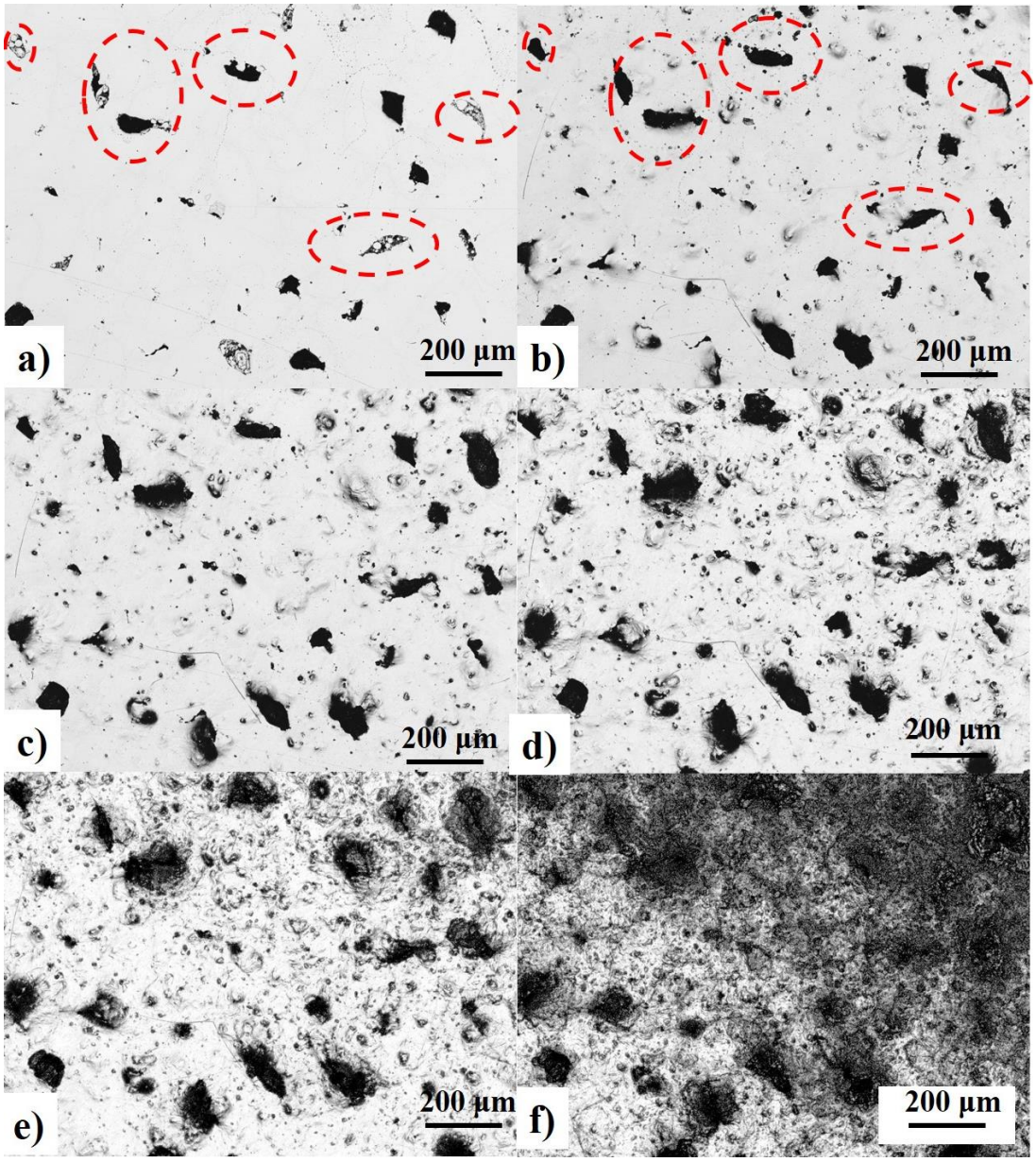

Fig. 11 Surface topography tracking of sample C SLM 2 observed at (a) the original state; (b) after 30 s; (c) after 1.5 min; (d) after 6 min; (e) after 30 min, and (f) after 190 min of cavitation erosion testing.

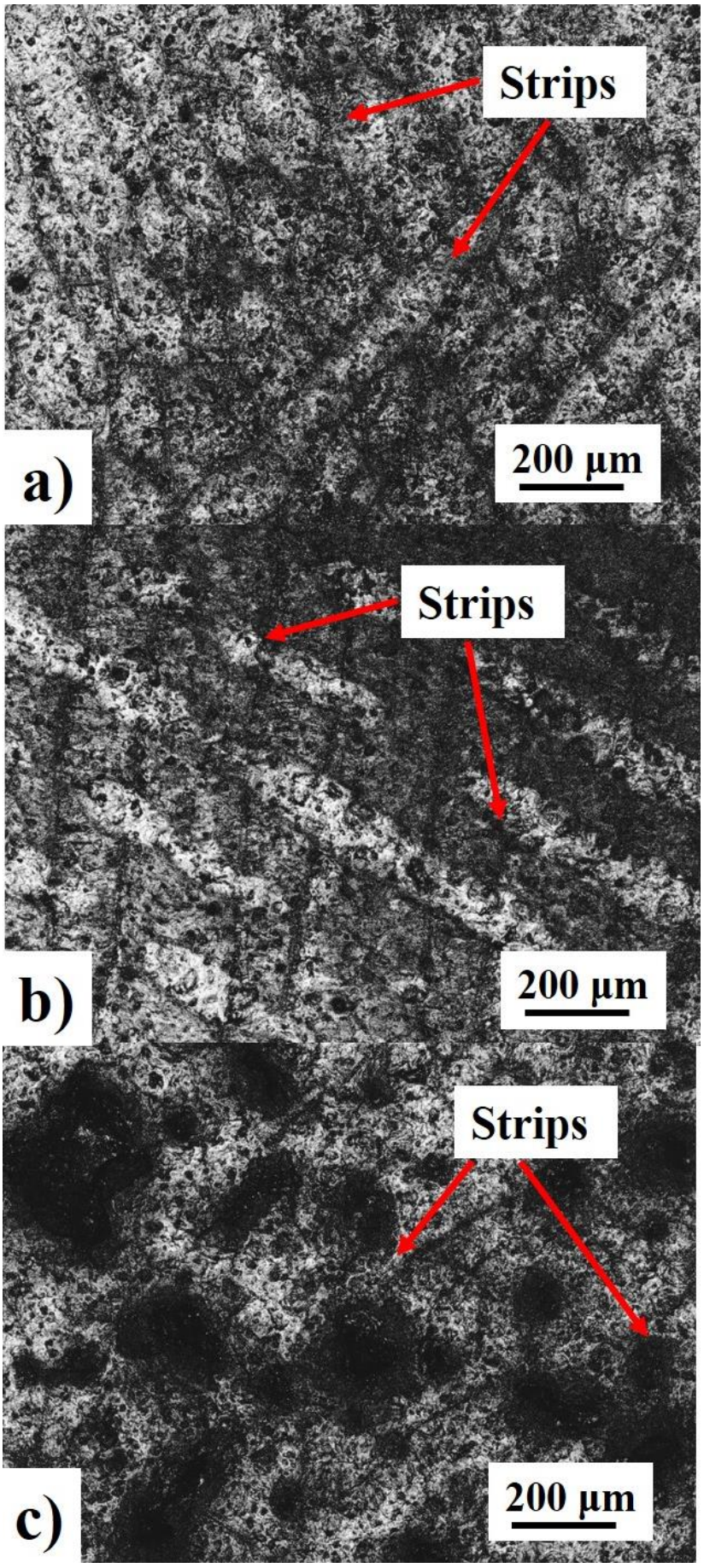
Strips
200 µm
a)
Strips
200 µm
b)
Strips
200 µm
c)

Fig. 12 CLSM graphs of strips observed after testing on samples: (a) A SLM 1; (b) B SLM 0.4, and (c) C SLM 2.

3.3 Surface topography

The changes in the surface topography of the same area on sample D are shown in Fig. 9. During the first 90 s, the number of small voids greatly increases with actual mass loss. After 20 min of testing, the surface is thoroughly damaged and becomes very rough. After 70 min of erosion testing, small craters start to connect, becoming large craters (Fig. 10c). At 100 min, a deep crater forms as shown in Fig. 10b. Fig. 10a shows that the crater has become very deep.

The changes in the surface topography of the same area on sample C are shown in Fig. 11. Comparing the surface topography after 30 s of testing (Fig, 11b) to the original state (Fig. 11a), the number of voids is greatly increased which is similar to sample D. However, some particles that have been inside the voids at the original state are no longer detectable after 30 s of erosion testing, which are marked with red circles in Figs. 11a and 11b. This phenomenon is not observed in sample D, which is believed to be the main reason for the extremely high erosion rate of SLM samples that is initially observed. After that, the number of voids increases slightly. Plastic deformation greatly effects the change of the surface topography. However, compared to sample D, plastic deformation on sample C is not severe and no large craters are observed. The other two SLM samples have exhibited similar behaviors, which are not shown. Some strips oriented in several directions are observed on the SLM samples which become obvious from 70 min of the erosion tests. Fig. 12 depicts those strips as observed after testing.

3.4 Cross-section observation

A cross-section of sample D after testing is shown in Fig. 13. The depth of a crater is greater than 200 μm, indicating a very high erosion rate. Fig. 13b indicates vertical plastic deformation which is also found in a previous study [9]. Cracks initiating both from the surface (Fig. 13c) and below the surface (Fig. 13d) are observed.

The cross-sections of the SLM samples are shown in Fig. 14. The surfaces of the SLM samples show mild damage in the cross section compared to that of sample D. The depth of the craters is less than 20 μm which is much less than that of sample D (Figs. 14 b, 14d, and 14f). Some cracks are also observed on sample B. They are connected to pores. These cracks are formed because of the SLM process

introduces thermal effects, as reported by Gu et al. [28], Yap et al. [29], and Uriondo et al. [16].

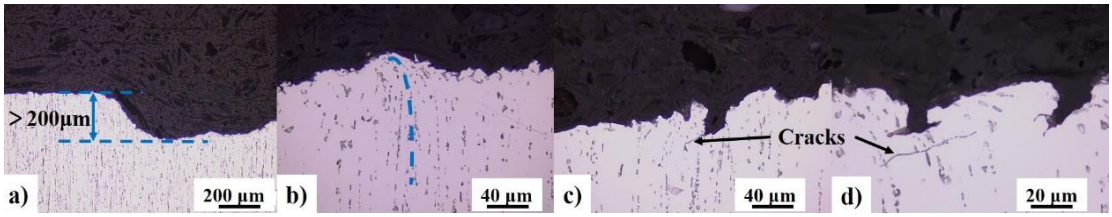

Fig. 13 CLSM graphs of cross section of sample D after tests. Figure a) shows that the erosion depth is more than 200 µm; figure b) shows the plastic deformation in the lateral direction; figure c) and d) shows cracks.

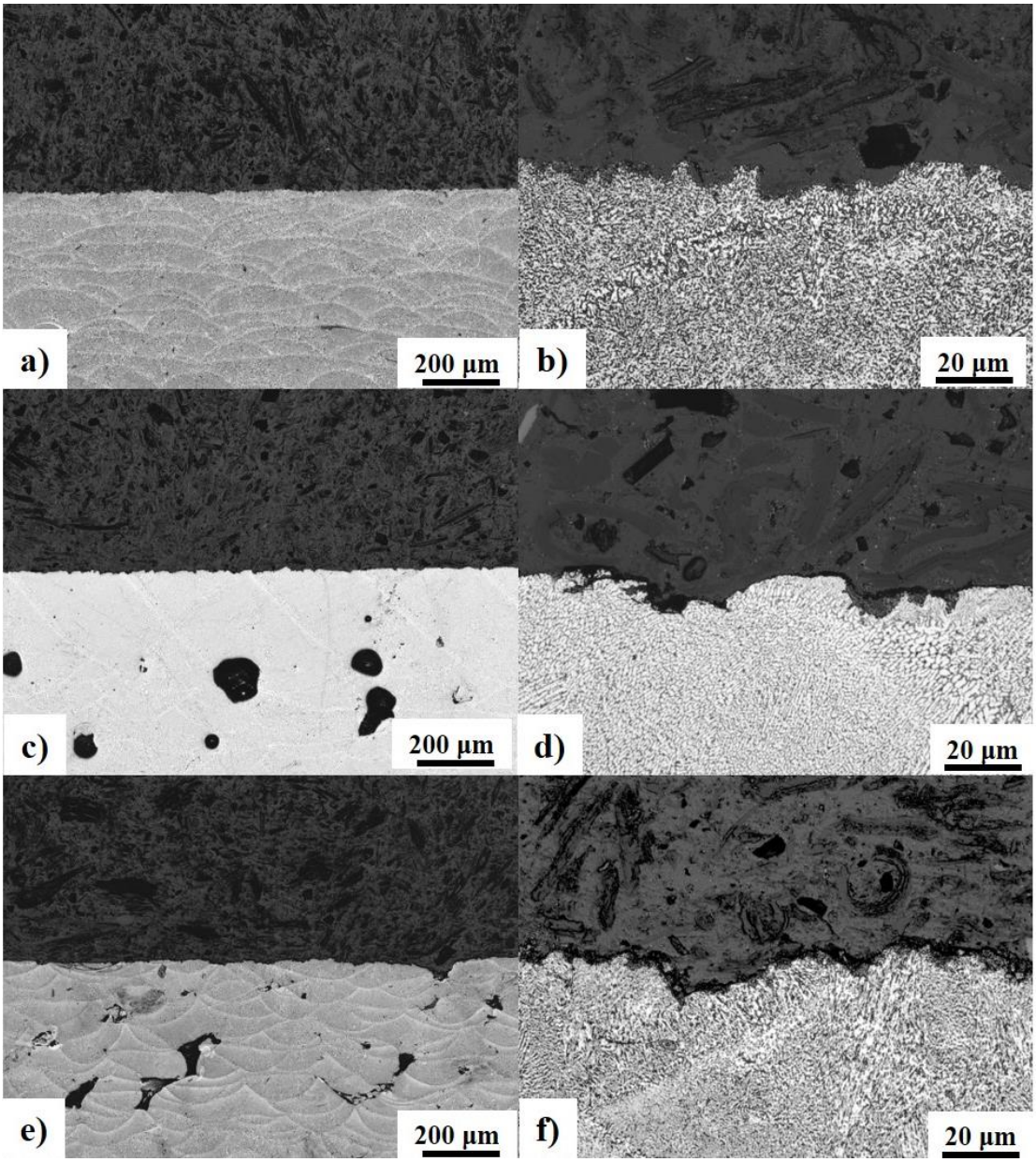

Fig. 14 CLSM graph of the cross section of the samples after testing at low and high magnification: (a) and (b) A SLM 1; (c) and (d) B SLM 0.4; (e) and (f) C SLM 2.

4. Discussion

4.1 Comparison between the SLM and the wrought samples

During SLM process, the laser focuses on a very small spot (50 μm in diameter). Thus, the temperature at the spot can be extremely high. On the other hand, the laser spot moves at a very high speed (from several hundred to several thousand mm/s) causing temperature to cool down rapidly. According to the FEM simulation, the temperature at the spot can be above 2000 ° C while the temperature of the substrate which is only 1 mm away from the spot is only approximately 100 ° C [30]. It causes very sharp temperature gradients and the materials undergo a rapid heating and cooling process leading to very fine and uniform grains, which is characterized by the SLM progress.

As shown in Fig. 4, SLM processed AlSi10Mg has a very fine microstructure, which renders the built component very hard. Kempen et al. [19] also reported that a SLM AlSi10Mg part had higher ultimate tensile strength and better elongation than a high pressure die casting part. These good mechanical properties are attributed to the high cavitation erosion resistance of the SLM AlSi10Mg parts. The SLM samples suffer from much less plastic deformation than the wrought sample.

4.2 Comparison among the SLM samples processed by different scanning speeds

The laser scanning speed is a very important parameter which decides the amount of the laser energy distributed to the materials. A low laser scanning speed indicates the laser energy input per unit time is increased, leading to a high melting temperature. It results in a large amount of powders becoming liquid and a long liquid lifetime. It further causes a considerably low liquid viscosity and resultant elevated thermal stresses which leads to the interruption of liquid film [31,32]. Therefore, pores and cracks are formed causing low density (e.g. sample B). On the other hand, the sample C processed by a high scanning speed also has a low density and many pores. Under such condition, the instability of the molten liquid is enhanced due to Marangoni convection leading to the spheroidization of the liquid within the molten pool (“balling” phenomenon). Balling effect results in the formation of discontinuous scan tracks and pores [26]. Therefore, it is difficult to fully densify the sample.

The optimization of the laser processing parameters, such as scanning speed, laser power, layer thickness, scanning strategy, and so on, is very difficult. According to the density measurement shown

in table 2, even a standard scanning speed was used, the sample A was still not fully densified. Therefore, all three SLM samples have pores. Increased number of pores reduces the material densification. The measurement of density shown in table. 2 indicates that the sample A has the highest density and the fewest pores while the sample B has the lowest density and the most pores. However, a quantitative study is required to study the relation between pores and density.

The presence of pores prohibits the continuity of scanning tracks leaving some unmelted powders inside pores. Moreover, too high scanning speed generates insufficient laser energy making some powders not melted. Too low scanning speed enhances balling effect which also increases the number of unmelted powders. Thus, all SLM samples have some particles inside pores while too low scanning speed or too high scanning speed will increase the number of unmelted particles.

During the cavitation erosion process, all SLM samples have very high mass loss in the beginning due to the removal of unmelted particles inside pores (shown in Fig. 11). Therefore, a sample with many pores is prone to suffer from the removal of particles which leads to a high mass loss. The cumulative mass loss shown in Fig. 7 is in accordance with such manner. The sample A with the highest density shows the lowest mass loss while the sample B with the lowest density shows the highest mass loss in the beginning of the erosion. During the steady-state period, the mass loss rate is independent of pores thus three samples have very close mass loss rates. In this period, the mass loss is irrelevant to the laser scanning speeds.

As a result, a sample processed by too high or too low scanning speeds tends to have many pores, which increase the mass loss in the beginning of the erosion tests. Reducing the number of pores and increasing the density of SLM parts is crucial since it can increase the erosion resistant particularly in the beginning of the erosion tests.

4.3 The influence of HAZ in the SLM samples

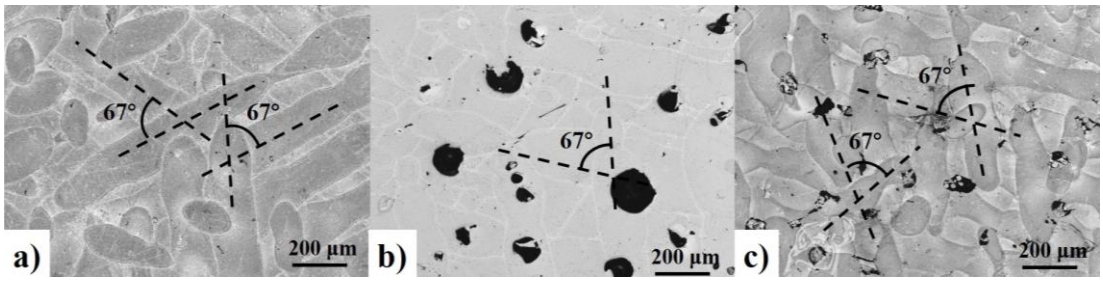

Fig. 15 Laser tracks in etched SLM surfaces: (a) sample A_SLM 1; (b) sample B_SLM 0.4; and (c) sample C_SLM 2.

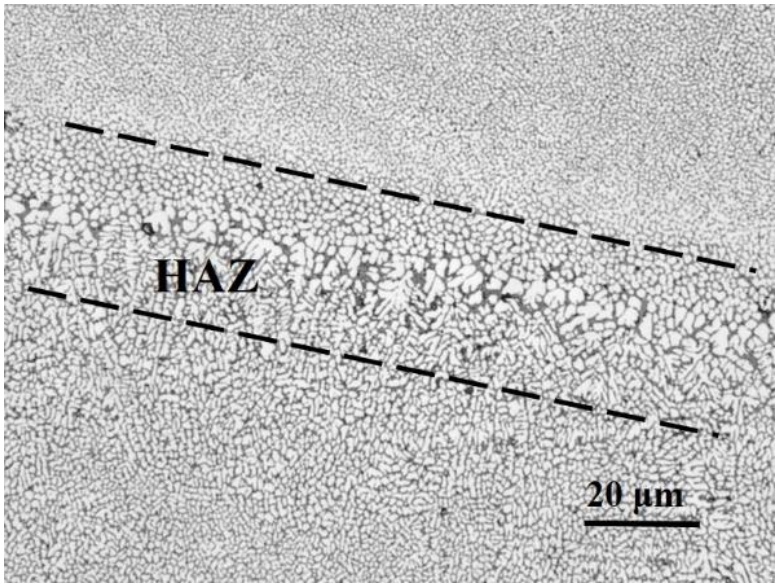

Fig. 16 A CLSM image showing HAZ on the surface of a new SLM sample.

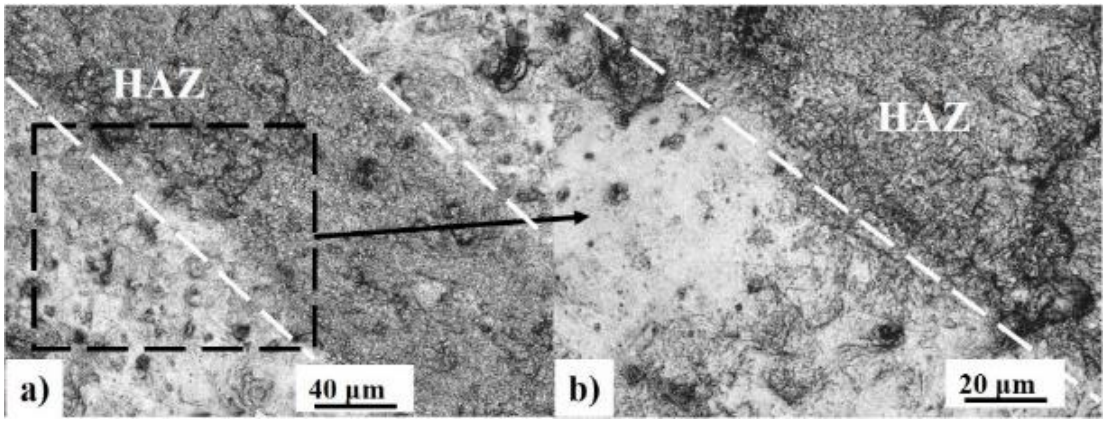

Fig. 17 CLSM images showing HAZ after cavitation erosion.

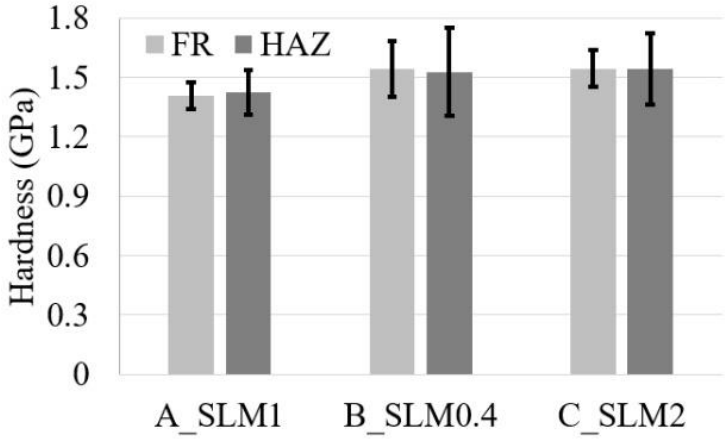

Fig. 18 Nano hardness (mean value and standard deviation) in three SLM samples. The indentation was performed six times at

each region.

Some strips were observed on the SLM samples From Fig. 15, these strips are the laser scanning tracks on different layers of powder. In order to produce a good connection between each layer, every layer was scanned with the tracks rotated over 67° to the previous layer. A closer observation is made by CLSM using 100 × magnitude, as shown in Fig. 16. The boundary of the scanning tracks shows large grains, which is known as the heat affected zone (HAZ). The formation of HAZ is due to the re-melting of the previous scanned track, as reported by other researchers [17,33]. Fig. 17 shows the eroded SLM surface. Results have shown that the surface topography in the HAZ becomes rougher than the other regions. According to the nano-hardness measurements shown in Fig. 18, there is no detectable difference between HAZ and fine grain zones (FZ). This suggests that the rough surface topography in the HAZ is probably due to the large spaces between grains in the HAZ (Fig. 16). These spaces are more likely to be plastically deformed. This matter requires further study.

5. Conclusions

The cavitation erosion behaviors of SLM processed AlSi10Mg parts with different laser scanning speeds were studied using ASTM G134 test set-up. Microstructures, hardness, and surface topography were examined. Cavitation erosion results were here presented and discussed. The study allows the following conclusions to be drawn:

- SLM samples have pores that cause reduced density. However, they also have a very fine cellular-dendritic structure, which leads to high hardness.
- The cavitation erosion rate of the SLM samples peaked at a very high level at first and then decreased significantly. The process was accompanied by the removal of particles in the pores.
- The erosion rate of the SLM samples was extremely low in the steady-state period, which was one tenth of that of the wrought sample. Moreover, the SLM samples undergo less plastic deformation than the wrought sample. High hardness and fine microstructure are attributed to the high erosion resistance of the SLM parts.
- Laser scanning speeds affect the sample density and the number of pores which further influence the maximum erosion rate.

Acknowledgements

This research was funded by the National Natural Science Foundation of China (Grant No. 51405431), Zhejiang Provincial Natural Science Foundation for Distinguished Young Scholars (No. LR15E050001), Fundamental Research Funds for the Central Universities (No. 2016FZA4003), the National Basic Research Program of China (973 Program, Grant Nos. 2013CB035400 and 2015CB058100), and the Zhejiang science and technology innovation team (Grant No. 2013TD01).

References

[1] K.-H. Kim, G.L. Chahine, J.-P. Franc, A. Karimi, Advanced experimental and numerical techniques for cavitation erosion prediction, 2014.

[2] S. Hattori, T. Hirose, K. Sugiyama, Prediction method for cavitation erosion based on measurement of bubble collapse impact loads, Wear. 269 (2010) 507–514. doi:10.1016/j.wear.2010.05.015.

[3] J.-K. Choi, A. Jayaprakash, G.L. Chahine, Scaling of cavitation erosion progression with cavitation intensity and cavitation source, Wear. 278-279 (2012) 53–61. doi:10.1016/j.wear.2012.01.008.

[4] H. Soyama, Effect of nozzle geometry on a standard cavitation erosion test using a cavitating jet, Wear. 297 (2013) 895–902. doi:10.1016/j.wear.2012.11.008.

[5] J.R. Laguna-Camacho, R. Lewis, M. Vite-Torres, J.V. Méndez-Méndez, A study of cavitation erosion on engineering materials, Wear. 301 (2013) 467–476. doi:10.1016/j.wear.2012.11.026.

[6] S. a. Karrab, M. a. Doheim, M.S. Aboraia, S.M. Ahmed, Study of Cavitation Erosion Pits on 1045 Carbon Steel Surface in Corrosive Waters, J. Tribol. 134 (2012) 011602. doi:10.1115/1.4005646.

[7] Z. Li, J. Han, J. Lu, J. Zhou, J. Chen, Vibratory cavitation erosion behavior of AISI 304 stainless steel in water at elevated temperatures, Wear. 321 (2014) 33–37. doi:10.1016/j.wear.2014.09.012.

[8] S.M. Ahmed, K. Hokkirigawa, O. Kazuo, Developing stages of ultrasonically produced

cavitation erosion and corresponding surface roughness, JSME Int. J. 33 (1990) 11–16.

[9] Y. Zhu, J. Zou, W.L. Zhao, X.B. Chen, H.Y. Yang, Tribology International A study on surface topography in cavitation erosion tests of AlSi10Mg, Tribiology Int. 102 (2016) 419–428. doi:10.1016/j.triboint.2016.06.007.

[10] J.H. Chen, W. Wu, Cavitation erosion behavior of Inconel 690 alloy, Mater. Sci. Eng. A. 489 (2008) 451–456. doi:10.1016/j.msea.2007.12.007.

[11] R. Cottam, V. Luzin, H. Moody, D. Edwards, A. Majumdar, Y.C. Wong, J. Wang, M. Brandt, The role of microstructural characteristics in the cavitation erosion behaviour of laser melted and laser processed Nickel-Aluminium Bronze, Wear. 317 (2014) 56–63. doi:10.1016/j.wear.2014.05.002.

[12] A. Al-Hashem, W. Riad, The role of microstructure of nickel-aluminium-bronze alloy on its cavitation corrosion behavior in natural seawater, Mater. Charact. 48 (2002) 37–41. doi:10.1016/S1044-5803(02)00196-1.

[13] M. Pohl, J. Stella, Quantitative CLSM roughness study on early cavitation-erosion damage, Wear. 252 (2002) 501–511. doi:10.1016/S0043-1648(02)00003-0.

[14] R.K. Kumar, S. Seetharamu, M. Kamaraj, Quantitative evaluation of 3D surface roughness parameters during cavitation exposure of 16Cr–5Ni hydro turbine steel, Wear. 320 (2014) 16–24. doi:10.1016/j.wear.2014.07.015.

[15] J. Li, B. Wu, H. Chen, Formation and development of iridescent rings around cavitation erosion pits, Tribol. Lett. 52 (2013) 495–500. doi:10.1007/s11249-013-0234-7.

[16] A. Uriondo, M. Esperon-miguez, S. Perinpanayagam, The present and future of additive manufacturing in the aerospace sector : A review of important aspects, 229 (2015) 2132–2147. doi:10.1177/0954410014568797.

[17] L. Thijs, K. Kempen, J.P. Kruth, J. Van Humbeeck, Fine-structured aluminium products with controllable texture by selective laser melting of pre-alloyed AlSi10Mg powder, Acta Mater. 61 (2013) 1809–1819. doi:10.1016/j.actamat.2012.11.052.

[18] D. Manfredi, F. Calignano, M. Krishnan, R. Canali, From Powders to Dense Metal Parts: Characterization of a Commercial AlSiMg Alloy Processed through Direct Metal Laser Sintering, (2013) 856–869. doi:10.3390/ma6030856.

[19] K. Kempen, L. Thijs, J. Van Humbeeck, J. Kruth, Mechanical properties of AlSi10Mg produced by Selective Laser Melting, 39 (2012) 439–446. doi:10.1016/j.phpro.2012.10.059.

[20] N. Read, W. Wang, K. Essa, M.M. Attallah, Selective laser melting of AlSi10Mg alloy: Process optimisation and mechanical properties development, Mater. Des. 65 (2015) 41–424.

[21] E. Brandl, U. Heckenberger, V. Holzinger, D. Buchbinder, Additive manufactured AlSi10Mg samples using Selective Laser Melting (SLM): Microstructure , high cycle fatigue , and fracture behavior, 34 (2012) 159–169. doi:10.1016/j.matdes.2011.07.067.

[22] Z. Sun, X. Tan, S. Tor, W.Y. Yeong, Selective laser melting of stainless steel 316L with low porosity and high build rates, 104 (2016) 197–204. doi:10.1016/j.matdes.2016.05.035.

[23] B. Zhang, C. Coddet, Selective Laser Melting of Iron Powder: Observation of Melting Mechanism and Densification Behavior Via Point-Track-Surface-Part Research, J. Manuf. Sci. Eng. 138 (2015) 051001. doi:10.1115/1.4031366.

[24] C. Qiu, C. Panwisawas, M. Ward, H.C. Basoalto, J.W. Brooks, M.M. Attallah, On the role of melt flow into the surface structure and porosity development during selective laser melting, Acta Mater. 96 (2015) 72–79. doi:10.1016/j.actamat.2015.06.004.

[25] L. Thijs, F. Verhaeghe, T. Craeghs, J. Van Humbeeck, J.P. Kruth, A study of the microstructural evolution during selective laser melting of Ti-6Al-4V, Acta Mater. 58 (2010) 3303–3312. doi:10.1016/j.actamat.2010.02.004.

[26] D. Gu, Y. Shen, Balling phenomena during direct laser sintering of multi-component Cu-based metal powder, J. Alloys Compd. 432 (2007) 163–166. doi:10.1016/j.jallcom.2006.06.011.

[27] M. Cabrini, S. Lorenzi, T. Pastore, S. Pellegrini, D. Manfredi, P. Fino, S. Biamino, C. Badini, Journal of Materials Processing Technology Evaluation of corrosion resistance of Al – 10Si – Mg alloy obtained by means of Direct Metal Laser Sintering, 231 (2016) 326–335.

[28] D. Gu, Y.-C. Hagedorn, W. Meiners, K. Wissenbach, R. Poprawe, Selective Laser Melting of in-situ TiC/Ti5Si3 composites with novel reinforcement architecture and elevated performance, Surf. Coatings Technol. 205 (2011) 3285–3292. doi:10.1016/j.surfcoat.2010.11.051.

[29] C.Y. Yap, C.K. Chua, Z.L. Dong, Z.H. Liu, D.Q. Zhang, L.E. Loh, S.L. Sing, Review of selective laser melting: Materials and applications, Appl. Phys. Rev. 2 (2015) 041101. doi:10.1063/1.4935926.

[30] C. Weingarten, D. Buchbinder, N. Pirch, W. Meiners, K. Wissenbach, R. Poprawe, Formation and reduction of hydrogen porosity during selective laser melting of AlSi10Mg, J. Mater. Process. Technol. 221 (2015) 112–120. doi:10.1016/j.jmatprotec.2015.02.013.

[31] D. Gu, Y.-C. Hagedorn, W. Meiners, G. Meng, R.J.S. Batista, K. Wissenbach, R. Poprawe, Densification behavior, microstructure evolution, and wear performance of selective laser melting processed commercially pure titanium, Acta Mater. 60 (2012) 3849–3860. doi:10.1016/j.actamat.2012.04.006.

[32] M. Zhong, H. Sun, W. Liu, X. Zhu, J. He, Boundary liquation and interface cracking characterization in laser deposition of Inconel 738 on directionally solidified Ni-based superalloy, 53 (2005) 159–164. doi:10.1016/j.scriptamat.2005.03.047.

[33] I. Rosenthal, A. Stern, N. Frage, Microstructure and Mechanical Properties of AlSi10Mg Parts Produced by the Laser Beam Additive Manufacturing (AM) Technology, Metallogr. Microstruct. Anal. 3 (2014) 448–453. doi:10.1007/s13632-014-0168-y.

Highlights:

- SLM samples have a fine cellular-dendritic structure and pores.
- SLM samples have an extremely high erosion rates in the beginning of the tests.
- The removal of unmelted particles inside pores was observed in the beginning.
- The erosion rate of SLM samples is very low in the steady-state period.
- Different scanning speeds influence sample densities and the max erosion rates.